catalysts

MDPI

Article

Carbon Quantum Dots (CQDs) Decorated Bi_2O_{3-x} Hybrid Photocatalysts with Promising NIR-Light-Driven Photodegradation Activity for AO7

Tao Xian [1,*], Xiaofeng Sun [1], Lijing Di [1], Yongjie Zhou [1], Jun Ma [1], Hongqin Li [1] and Hua Yang [2]

[1] College of Physics and Electronic Information Engineering, Qinghai Normal University, Xining 810008, China; sunxf027@126.com (X.S.); woshidilijing99@163.com (L.D.); zyj509612@163.com (Y.Z.); mjun7302@163.com (J.M.); lhq18195787657@126.com (H.L.)

[2] State Key Laboratory of Advanced Processing and Recycling of Non-ferrous Metals, Lanzhou University of Technology, Lanzhou 730050, China; hyang@lut.cn

* Correspondence: xiantao1204@163.com; Tel.: +86-971-6307633

Received: 12 November 2019; Accepted: 1 December 2019; Published: 6 December 2019

Abstract: In this work, Bi_2O_{3-x} with surface oxygen vacancies was prepared through the $NaBH_4$ reduction of Bi_2O_3. After that, carbon quantum dots (CQDs) were deposited onto the surface of the Bi_2O_{3-x} to obtain a series of the CQDs/Bi_2O_{3-x} composites. The HRTEM and XPS characterizations of the CQDs/Bi_2O_{3-x} composites suggest that the thickness of surface oxygen vacancies could be adjusted by changing the concentration of $NaBH_4$ solution, and the intimate contact between CQDs and the Bi_2O_{3-x} is achieved. Acid orange 7 (AO7) was adopted as the target reactant for investigating the photocatalytic degradation activities of the CQDs/Bi_2O_{3-x} composites under simulated sunlight and NIR light irradiation. It is found that the photocatalytic activities of the samples are closely related to the concentration of $NaBH_4$ and content of CQDs. The Bi_2O_{3-x} samples exhibit enhanced simulated-sunlight-driven photocatalytic activity compared with Bi_2O_3. Specifically, the optimal degradation efficiency of AO7 is achieved over the 3R-Bi_2O_{3-x} (concentration of $NaBH_4$: 3 mmol/L), which is 1.38 times higher than the degradation AO7 efficiency over Bi_2O_3. After the decoration of the 3R-Bi_2O_{3-x} surface with CQDs, the simulated-sunlight-driven photocatalytic activity of the CQDs/Bi_2O_{3-x} composite could be further enhanced. Among the samples, the 15C/3R-Bi_2O_{3-x} sample reveals the highest photocatalytic activity, leading to an AO7 degradation percentage of ~97% after 60 min irradiation. Different from Bi_2O_3 and the 3R-Bi_2O_{3-x}, the 15C/3R-Bi_2O_{3-x} sample also exhibits near-infrared (NIR)-light-driven photocatalytic degradation activity. In addition, the intrinsic photocatalytic activity of CQDs/Bi_2O_{3-x} composite was further confirmed by the degradation of phenol under simulated sunlight and NIR light irradiation. The photocurrent response and electrochemical impedance spectroscopy (EIS) measurements confirm the efficient migration and separation of photogenerated charges in the CQDs/Bi_2O_{3-x} samples. The •OH and h^+ are proved to be the main reactive species in the simulated sunlight and NIR light photocatalytic processes over the CQDs/Bi_2O_{3-x} composites. According to the above experiments, the photocatalytic degradation mechanisms of the CQDs/Bi_2O_{3-x} composites under simulated sunlight and NIR light illumination were proposed.

Keywords: Bi_2O_3; photocatalytic; oxygen vacancies; CQDs; composites

1. Introduction

Recently, bismuth-based photocatalysts have been widely investigated owing to their promising application in wastewater purification [1–5]. In comparison with the famous photocatalyst TiO_2 and ZnO [6,7], bismuth-based photocatalysts generally have relatively smaller bandgap energy and exhibit interesting visible-light response ability. As one of important bismuth-containing photocatalysts, bismuth oxide (Bi_2O_3) has attracted considerable attention for the photocatalytic degradation of organic pollutants and reduction of Cr (VI) owing to its narrow band gap and non-toxicity [8–16]. Generally, Bi_2O_3 exhibits six different crystalline phases denoted as α-, β-, γ-, δ-, ω-, ε-Bi_2O_3 [12–18]. Among them, α-Bi_2O_3 photocatalyst has been frequently studied because of its good structure stability and deep valence band [19–24]. However, the photocatalytic activity of bare Bi_2O_3 is unsatisfactory for practical application due to the high recombination rate of photogenerated electrons and holes. Furthermore, the absorption of near-infrared (NIR) light is a key point for the enhancement of utilization efficiency of solar energy [25,26]. To promote the separation of photogenerated charges and expand the photoresponse range, several methods have been used to modify Bi_2O_3 [27–30].

As we know, the introduction of oxygen vacancies on the surface of photocatalysts is regarded as an important and promising strategy to inhibit the recombination of photogenerated charges and extend the light absorption range [31–35]. It has been demonstrated that the surface oxygen vacancies can work as excellent photogenerated charges receivers and adsorption sites of species, thereby obviously promoting the migration of photoinduced charges to the adsorbed species [33]. The separation efficiency of photogenerated charges can be improved during this process. On the other hand, the induced surface oxygen vacancies can narrow band gap of photocatalysts, which extends their photoresponse range [33]. Until now, only a few works have been focused on the investigation of photocatalytic performance of Bi_2O_3 with surface oxygen vacancies. Liu et al. reported a hydrogenation method to introduce the oxygen vacancies on the surface of Bi_2O_3, thus improving its photocatalytic activity [30]. However, this method is suffered from harsh synthetic conditions and expensive facilities.

Carbon quantum dots (CQDs) are important class of nanocarbon materials, which exhibit good application prospect owing to its large surface area, non-toxicity, favorable biocompatibility, good water solubility, credible chemical stability, excellent electrical conductivity and unique up-converted photoluminescence property [36,37]. In particular, the excellent electron-accepting and -donating properties of photoexcited CQDs make it a promising candidate as a photosensitizer for the construction of nanocomposite photocatalysts with high separation efficiency of photogenerated charges [38–42]. Moreover, the outstanding up-converted photoluminescence property of CQDs provides an efficient way to generate short-wavelength emission light (from 350 to 750 nm) under the excitation of long-wavelength light (NIR light, from 800 to 1000 nm) [42]. The up-converted emission light can in turn excite the decorated photocatalysts to generate photoexcited charges, and thus their photoresponse region is extended. Therefore, the combination of the CQDs and photocatalysts is considered to be an ideal strategy to obtain excellent hybrid composite photocatalysts [38–42]. For Bi_2O_3, Sharma et al. reported the fabrication of the CQDs/Bi_2O_3 nanocoposites and their improved visible-light photocatalytic degradation activity [43]. Considering the advantages of the above modification methods, it is expected that efficient Bi_2O_3 photocatalysts with wide photoresponse regions can be obtained through the synergetic modification of surface oxygen vacancies and CQD decoration. To the best of our knowledge; however, the photocatalytic activities of CQD-decorated Bi_2O_{3-x} have not been reported yet.

In this work, the Bi_2O_{3-x} with surface oxygen vacancies was firstly prepared by a simple $NaBH_4$ reduction route, followed by the decoration of CQDs through a hydrothermal route to obtain the CQDs/Bi_2O_{3-x} composites. The photocatalytic acid orange 7 (AO7) and phenol degradation activity of the CQDs/Bi_2O_{3-x} composites under simulated sunlight and NIR light irradiation was studied. Furthermore, the corresponding photocatalytic mechanism was also proposed.

2. Results and Discussion

2.1. XRD and FTIR Analysis

The XRD patterns of pristine Bi_2O_3, 6R-$Bi_2O_{3\text{-}x}$ and 30C/3R-$Bi_2O_{3\text{-}x}$ are shown in Figure 1. All the diffraction peaks of pristine Bi_2O_3 can be perfectly indexed to monoclinic structure of α-Bi_2O_3, indicating the production of high-quality Bi_2O_3. Notably, the 6R-$Bi_2O_{3\text{-}x}$ and 30C/3R-$Bi_2O_{3\text{-}x}$ samples exhibit similar diffraction patterns to that of pristine Bi_2O_3, suggesting that the introduction of the CQDs and $NaBH_4$ reduction treatment does not lead to remarkable change in the crystal phase of Bi_2O_3. Moreover, no characteristic diffraction peaks of the CQDs are observed, which can be ascribed to their low content and weak diffraction peaks intensity. The existence of CQDs in the composite is further confirmed by FTIR investigation.

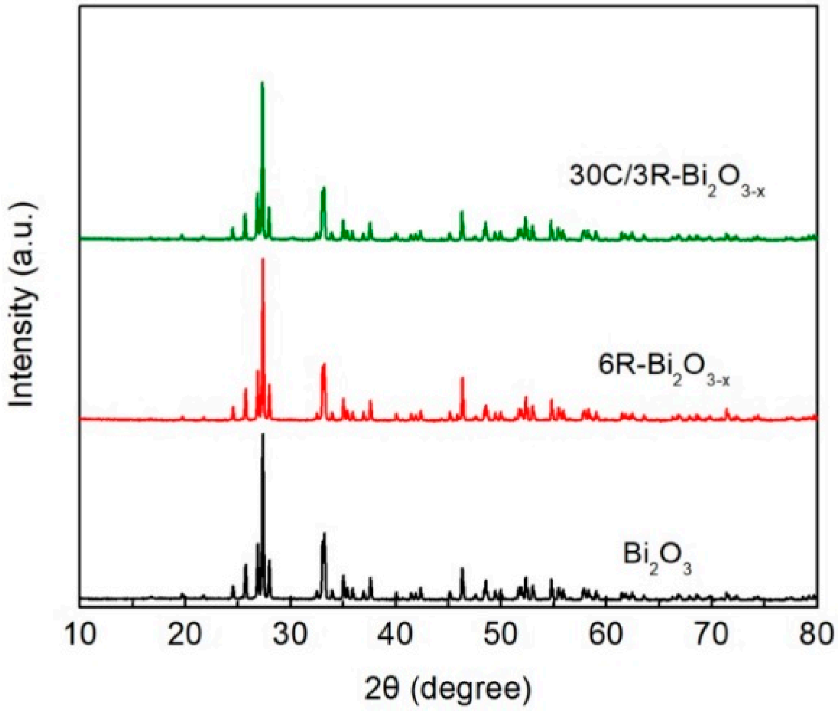

Figure 1. X-ray powder diffraction (XRD) patterns of Bi_2O_3, 6R-$Bi_2O_{3\text{-}x}$ and 30C/3R-$Bi_2O_{3\text{-}x}$ samples.

Figure 2 presents the FTIR spectra of Bi_2O_3 and 15C/3R-$Bi_2O_{3\text{-}x}$. In the case of pristine Bi_2O_3, the peaks at 431, 509 and 525 cm^{-1} can be assigned to the vibrations of Bi-O bonds in α-Bi_2O_3 [44–46]. For the spectrum of the 15C/3R-$Bi_2O_{3\text{-}x}$ sample, the characteristic peaks of Bi_2O_3 are also detected, and the deformation vibration of C-H (~635 cm^{-1}), the stretching vibration of C-C (~1630 cm^{-1}) and the stretching vibration of C-OH (~1120 cm^{-1}) are found [47,48]. This demonstrates the presence of CQDs in the composite. Furthermore, the absorption peaks at ~1380 cm^{-1} in the two samples belong to the O-H stretching vibration from the absorbed H_2O molecules [49].

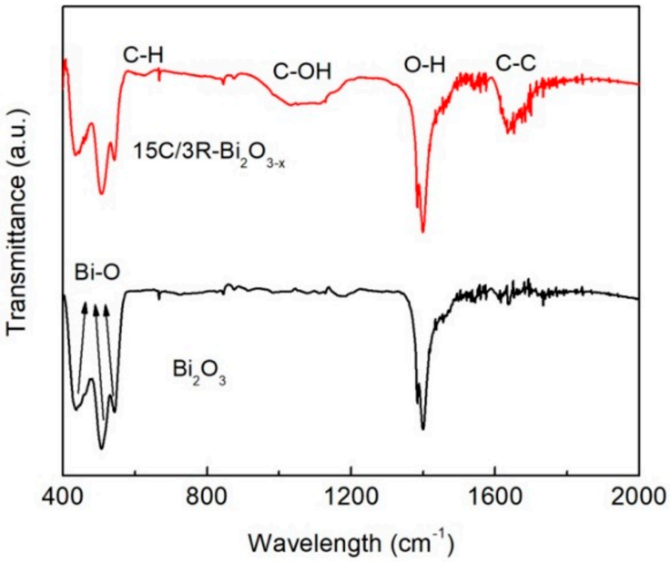

Figure 2. Fourier transform infrared spectra (FTIR) of Bi_2O_3 and 15C/3R-Bi_2O_{3-x} samples.

2.2. Morphology Observation

Figure 3a shows the TEM image of pristine Bi_2O_3, revealing that Bi_2O_3 exhibits an irregular spindle-like shape about several micrometers in size. From the high-resolution TEM (HRTEM) image of Bi_2O_3 (Figure 3b), we can see that pure Bi_2O_3 is well-crystallized and displays obvious lattice fringes throughout the whole particles. After reduced by 3 mmol/L $NaBH_4$ (Figure 3c), the edge of the 3R-Bi_2O_{3-x} sample becomes disorder and the thickness of the disordered layer is in the range from 10 to 15 nm, while the core area still exhibits a highly crystalline nature. This result suggests that the $NaBH_4$ treatment destroys the surface crystalline structure of Bi_2O_3 and leads to the generation of a disordered surface layer. Increasing the concentration of $NaBH_4$ to 6 mmol/L (Figure 3d), one can see that the thickness of disordered layer for the 6R-Bi_2O_{3-x} sample is found to be ~40 nm, which indicates that the thickness of the disordered layer trends to increase with the increase of concentration of $NaBH_4$. Figure 3e displays the TEM image of the CQDs, revealing that the CQDs displays a sphere-like shape and have a diameter of 10–15 nm. From the HRTEM image of 15C/3R-Bi_2O_{3-x} (Figure 3f), it is found that the CQDs with amorphous feature are decorated on the surface of 3R-Bi_2O_{3-x}. The structure of the disordered layer and the inner crystalline phase do not undergo detectable alteration during the hydrothermal decoration process of CQDs.

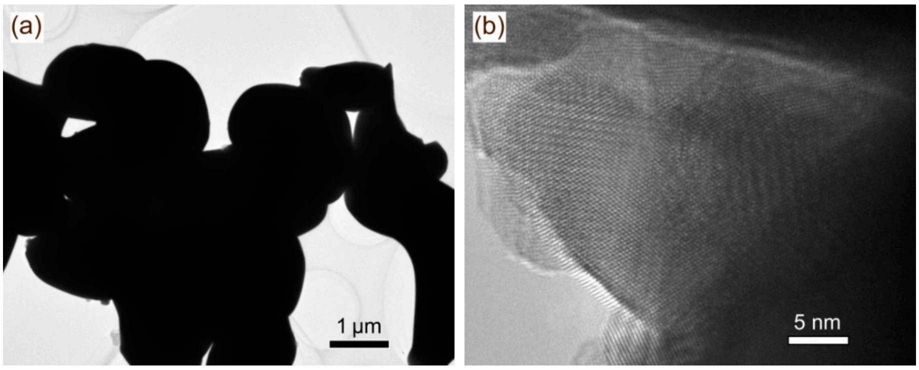

Figure 3. *Cont.*

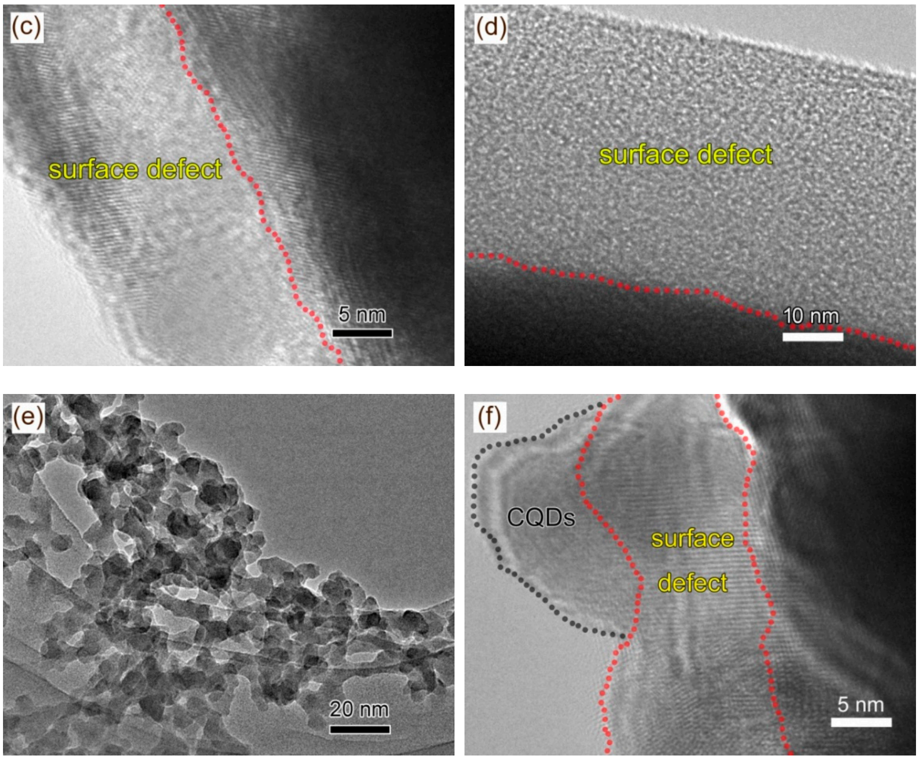

Figure 3. (**a**,**b**) Transmission electron microscopy (TEM) image and high-resolution (HR)TEM images of Bi_2O_3, respectively; (**c**,**d**) HRTEM images of the 3R-Bi_2O_{3-x} and 6R-Bi_2O_{3-x} samples, respectively; (**e**) TEM image of CQDs; (**f**) HRTEM image of the 15C/3R-Bi_2O_{3-x} sample.

The energy-dispersive X-ray (EDX) element mapping technique was employed to study the element distribution of the 15C/3R-Bi_2O_{3-x} sample. The dark-field scanning TEM (DF-STEM) image of the15C/3R-Bi_2O_{3-x} sample is presented in Figure 4a, and its corresponding elemental mappings are displayed in Figure 4b–d. It is found that Bi, O and C elements are uniformly distributed throughout the microparticles, which further demonstrates that the CQDs are decorated on the surface of the 3R-Bi_2O_{3-x}.

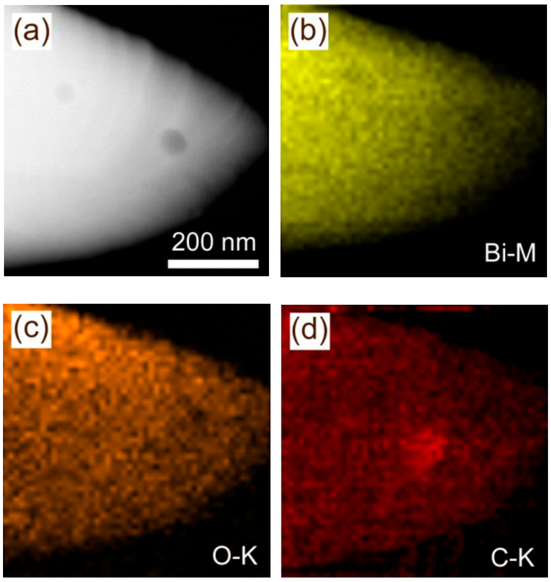

Figure 4. (**a**) Dark-field scanning TEM (DF-STEM) image of the 15C/3R-Bi_2O_{3-x} sample; (**b**–**d**) The corresponding energy dispersive X-ray elemental mapping images.

2.3. XPS Analysis

Figure 5 displays the XPS spectra of Bi_2O_3 and 15C/3R-Bi_2O_{3-x}. In the high-resolution XPS spectra of Bi 4f (Figure 5a), the strong peaks at binding energies of ~164.1 and ~159.2 eV for the two samples are assigned to the Bi $4f_{5/2}$ and Bi $4f_{7/2}$, respectively, demonstrating that Bi ion exhibits +3 oxidation state. The high-resolution XPS spectra of O 1s for Bi_2O_3 and 15C/3R-Bi_2O_{3-x} are displayed in Figure 5b,c, respectively. The broad signal of O 1s can be fitted into two peaks at ~529.8 and ~531.0 eV. The peak at ~529.8 eV belongs to the lattice oxygen, and another peak at ~531.0 eV is ascribed to the chemisorbed oxygen resulting from oxygen vacancies [50,51]. Generally, the destruction of the long-range order of lattice at the surface of the oxide particles gives rise to the generation of oxygen vacancies. It is found that the peak of oxygen vacancies for the 15C/3R-Bi_2O_{3-x} sample is much higher than that of Bi_2O_3. This reveals that the $NaBH_4$ reduction results in more oxygen vacancies at the surface of Bi_2O_3. In the XPS spectrum of C 1s for the 15C/3R-Bi_2O_{3-x} sample (Figure 5d), the peak of C 1s can be divided into two peaks at ~284.8 and ~288.3 eV, belonging to C-C bond with sp^2 orbital and oxygenated carbon, respectively, which demonstrates the existence of CQDs in the composite.

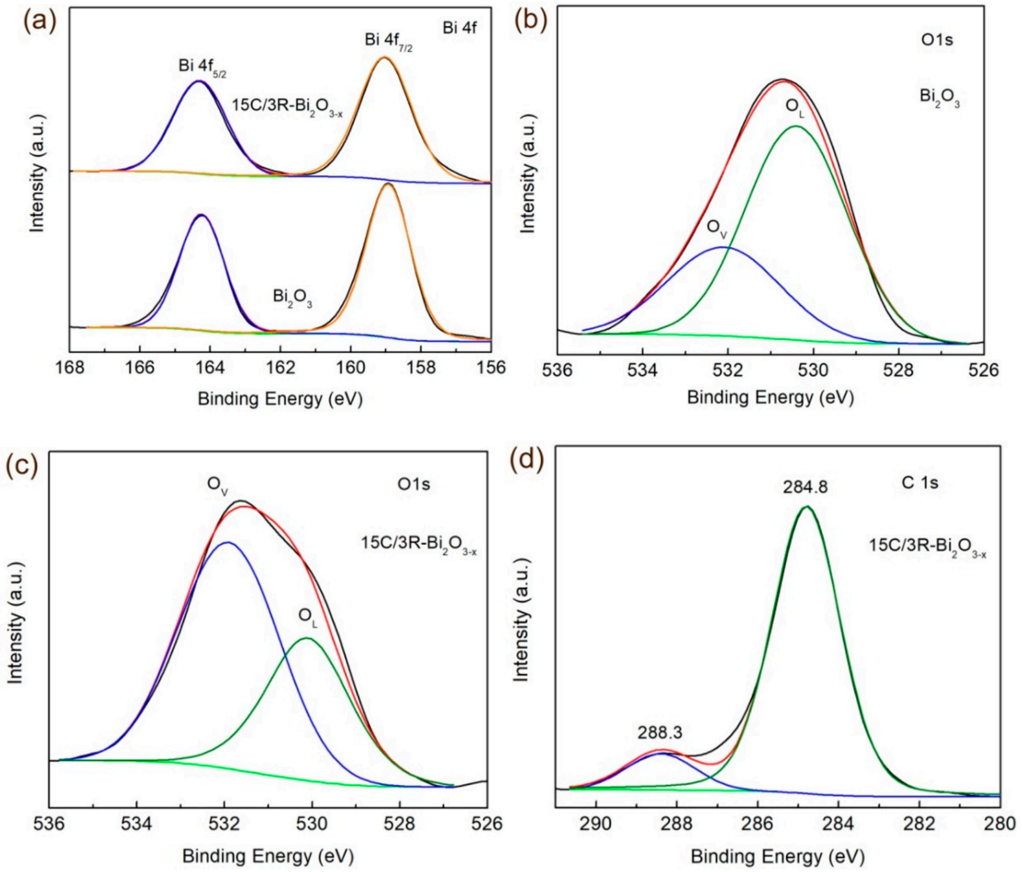

Figure 5. High-resolution X-ray photoelectron spectroscopy (XPS) spectra of Bi_2O_3 and 15C/3R-Bi_2O_{3-x} samples (**a**) Bi 4f; (**b**) and (**c**) O1s; (**d**) C 1s.

2.4. Optical Absorption Property

It is generally accepted that the physical properties of nanomaterials are highly related to their light absorption characteristics [52,53]. The UV-vis diffuse reflectance spectra of the Bi_2O_3 and Bi_2O_{3-x} samples are presented in Figure 6a. It is seen that pristine Bi_2O_3 displays obvious light absorption in the range from 300 to ~450 nm. After the $NaBH_4$ reduction treatment, the light absorbance of the Bi_2O_{3-x} samples exhibits a continuous increase with increasing $NaBH_4$ concentration. Figure 6b presents the corresponding first derivative spectra of Figure 6a, where the peak wavelength is determined to be the absorption edge of the samples [54,55]. The absorption edge of pristine Bi_2O_3 is found at

~429 nm. Meanwhile, the absorption edges of the $Bi_2O_{3\text{-}x}$ samples undergo a redshift from ~429 nm to ~441 nm compared with Bi_2O_3. According to the absorption edges, the band gaps of Bi_2O_3, 1R-$Bi_2O_{3\text{-}x}$, 1.5R-$Bi_2O_{3\text{-}x}$, 3R-$Bi_2O_{3\text{-}x}$ and 6R-$Bi_2O_{3\text{-}x}$ are separately estimated to be ~2.89, ~2.85, ~2.86, ~2.83 and ~2.81 eV.

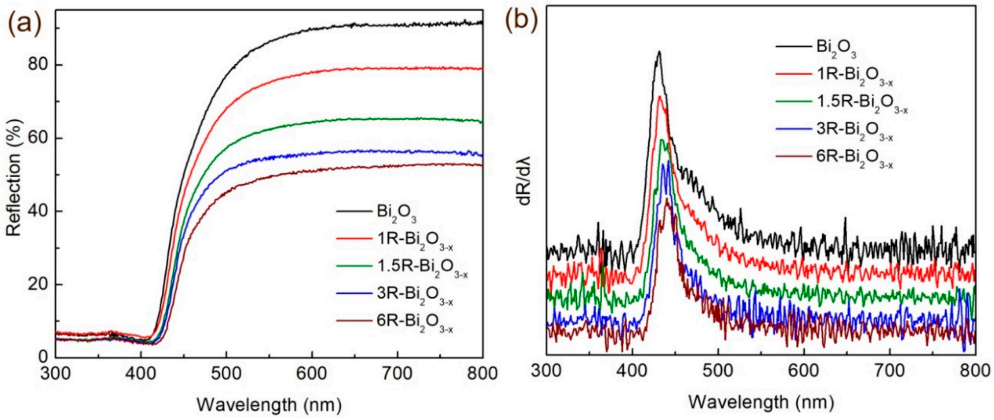

Figure 6. (**a**) UV-vis diffuse reflectance spectra of Bi_2O_3 and $Bi_2O_{3\text{-}x}$ samples; (**b**) the corresponding first derivative of the diffuse reflectance spectra.

Figure 7a,b presents the UV-vis diffuse reflectance spectra and corresponding first derivative spectra of the 3R-$Bi_2O_{3\text{-}x}$ and CQDs/$Bi_2O_{3\text{-}x}$ samples, respectively. In contrast to the 3R-$Bi_2O_{3\text{-}x}$ sample, the light absorption intensity of CQDs decorated 3R-$Bi_2O_{3\text{-}x}$ samples remarkably increases with the increase of the CQDs content in the samples. In addition, there is no obvious shift of absorption edge for the CQDs/$Bi_2O_{3\text{-}x}$ samples compared with 3R-$Bi_2O_{3\text{-}x}$, suggesting that the influence of CQDs on the band gap structure of $Bi_2O_{3\text{-}x}$ can be ignored.

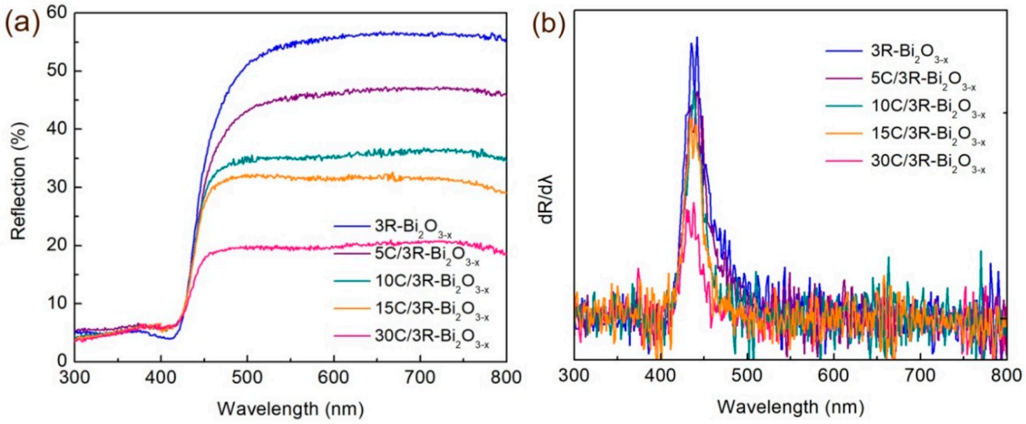

Figure 7. (**a**) UV-vis diffuse reflectance spectra of 3R-$Bi_2O_{3\text{-}x}$ and CQDs/$Bi_2O_{3\text{-}x}$ samples; (**b**) the corresponding first derivative of the diffuse reflectance spectra.

2.5. Photocatalytic Measurement

To explore the photocatalytic degradation performance of the catalysts, the AO7 was selected as a target reactant. Figure 8a presents the photocatalytic degradation curves of AO7 on Bi_2O_3 and $Bi_2O_{3\text{-}x}$ samples under simulated sunlight irradiation. Before photocatalytic reaction, the photolysis experiment in the absence of photocatalysts and adsorption experiment in dark were performed. It is found that the self-degradation of AO7 can be negligible after 60 min illumination, and no obvious adsorption of AO7 is detected. During the photocatalytic reaction, about ~54% of AO7 is degraded when using pristine Bi_2O_3 as the photocatalyst. After the $NaBH_4$ reduction, the degradation efficiency of the dye over the $Bi_2O_{3\text{-}x}$ samples gradually increases with increasing the $NaBH_4$ concentration, and the optimal degradation efficiency is achieved by the 3R-Bi_2O_{3-x} sample, which is 1.38 times higher than that photodegraded by pure Bi_2O_3. With further increase of the $NaBH_4$ concentration, however, the degradation percentage of the dye over the $NaBH_4$-treated Bi_2O_{3-x} samples undergoes a remarkable decrease. This can be attributed to the fact that bulk oxygen vacancies may be generated in Bi_2O_3 after high-concentration $NaBH_4$ reduction, which usually work as recombination centers of photoinduced charges. Figure 8b shows the UV-vis absorption spectra of AO7 solution over the 3R-Bi_2O_{3-x} sample during photocatalytic process, indicating that the intensity of characteristic peak for AO7 reduces with increasing the irradiation time. To further demonstrate the intrinsic photocatalytic property of Bi_2O_{3-x} sample, phenol is employed as another colorless target pollutant to evaluate the photocatalytic degradation activity of Bi_2O_3 and 3R-Bi_2O_{3-x} sample [56,57], as presented in Figure 8c. The photolysis experiment suggests that almost no degradation of phenol is observed in the absence catalysts under simulated sunlight irradiation. It is found that the introduction of Bi_2O_3 leads to phenol degradation percentage of ~21%. When 3R-Bi_2O_{3-x} sample is used as photocatalyst, the degradation percentage of phenol undergoes an obvious increase, and about 42% of phenol is degraded after 60 min irradiation. This reveals that the degradation of dye over Bi_2O_{3-x} sample is mainly ascribed to its intrinsic photocatalytic activity instead of dye sensitization. Considering the practical application of photocatalysts, it is necessary to clarify the photocatalytic reusability of the Bi_2O_{3-x} samples. Figure 8d shows the recycling photocatalytic degradation activity of 3R-Bi_2O_{3-x} for the degradation of AO7 under simulated sunlight irradiation. It is observed that the 3R-Bi_2O_{3-x} sample possesses good photocatalytic reusability with the degradation percentage of the dye remaining at over ~70% after 3 successive cycles.

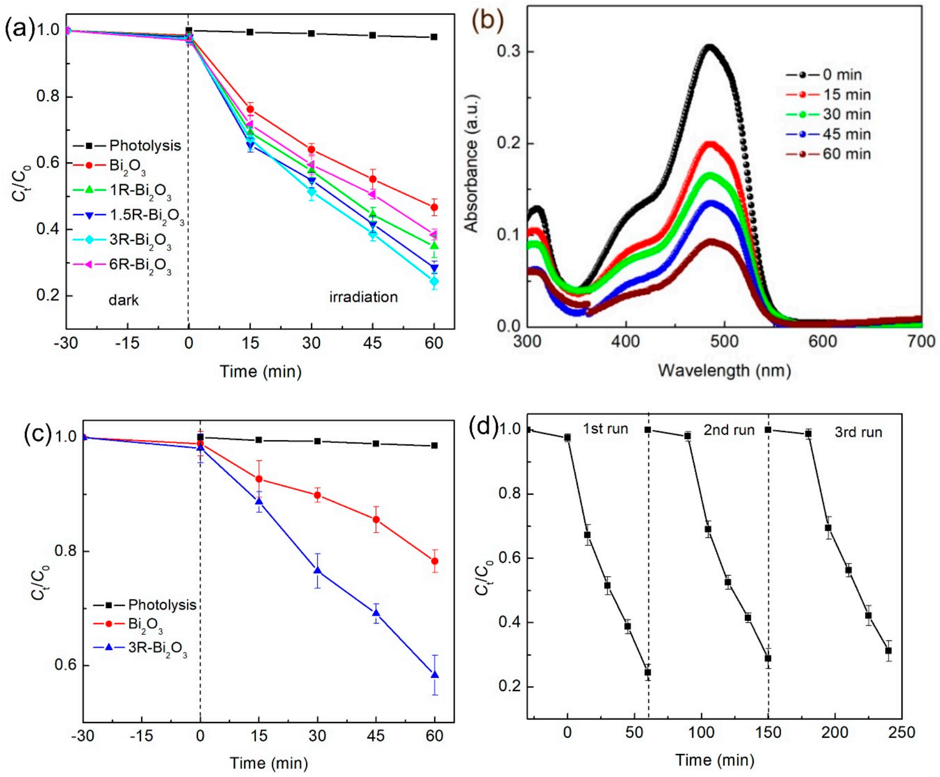

Figure 8. (**a**) Time-dependent photocatalytic degradation of AO7 using Bi_2O_3 and Bi_2O_{3-x} samples under simulated sunlight irradiation; (**b**) UV-vis absorption spectra of AO7 degraded by the 3R-Bi_2O_{3-x} sample under simulated sunlight irradiation; (**c**) Time-dependent photocatalytic degradation of phenol using Bi_2O_3 and 3R-Bi_2O_{3-x} samples under simulated sunlight irradiation; (**d**) Photocatalytic degradation of AO7 over the 3R-Bi_2O_{3-x} sample during three cycles under simulated sunlight irradiation. Initial conditions: *C*(catalysts) = 0.5 g/L, *C*(phenol) = 5 mg/L, *C* (AO7) = 5 mg/L, pH(AO7) ≈ 6.7, pH(phenol) ≈ 6.2, volume of reaction solution = 200 mL.

The simulated-sunlight-driven photocatalytic degradation performances of the CQDs/Bi_2O_{3-x} samples are shown Figure 9a. Figure 9b displays the UV-vis absorption spectra of AO7 with the increase of simulated sunlight irradiation time using the 15C/3R-Bi_2O_{3-x} sample as photocatalyst. It is seen that all the CQDs/3R-Bi_2O_{3-x} samples have higher photocatalytic activities than 3R-Bi_2O_{3-x}, and the AO7 degradation percentage closely correlates with the content of CQDs in the composites. The degradation percentage of AO7 first increases with the raise of CQDs content, then slightly decreases with further raise of CQDs content. Among them, the 15C/3R-Bi_2O_{3-x} sample presents an optimal photocatalytic activity. This result is mainly because excessive CQDs covering on the surface of 3R-Bi_2O_{3-x} particles are more likely to shield 3R-Bi_2O_{3-x} from light absorption. The photocatalytic degradation of AO7 over Bi_2O_3, 3R-Bi_2O_{3-x} and 15C/3R-Bi_2O_{3-x} sample under NIR light irradiation is also investigated, as shown in Figure 9c. Figure 9d presents the UV-vis absorption spectra of AO7 with the increase of NIR light irradiation time over the 15C/3R-Bi_2O_{3-x} sample. It is found that the degradation of the dye over pristine Bi_2O_3 and 3R-Bi_2O_{3-x} is negligible because they cannot be excited by NIR light (as evidenced by Figure 6a). Whereas the 15C/3R-Bi_2O_{3-x} sample exhibits obvious NIR-light-driven photocatalytic activity under same conditions, which is mainly caused by the decoration of CQDs. The intrinsic photocatalytic property of CQDs/3R-Bi_2O_{3-x} sample is also investigated. Figure 9e,f presents the degradation percentage of phenol over 15C/3R-Bi_2O_{3-x} sample under simulated sunlight and NIR light irradiation, respectively. During the simulated-sunlight-driven photocatalytic process, the degradation percentage of phenol over 15C/3R-Bi_2O_{3-x} sample reaches about 58% after 60 min of exposure. On the other hand, just ~16% of phenol is degraded by the 15C/3R-Bi_2O_{3-x} sample with 60 min of NIR light irradiation. Figure 9g,h shows the photocatalytic degradation reusability of the 15C/3R-Bi_2O_{3-x} sample under simulated sunlight and NIR light irradiation, respectively. It is seen that, in both cases, the 15C/3R-Bi_2O_{3-x} sample has stable photodegradation activity.

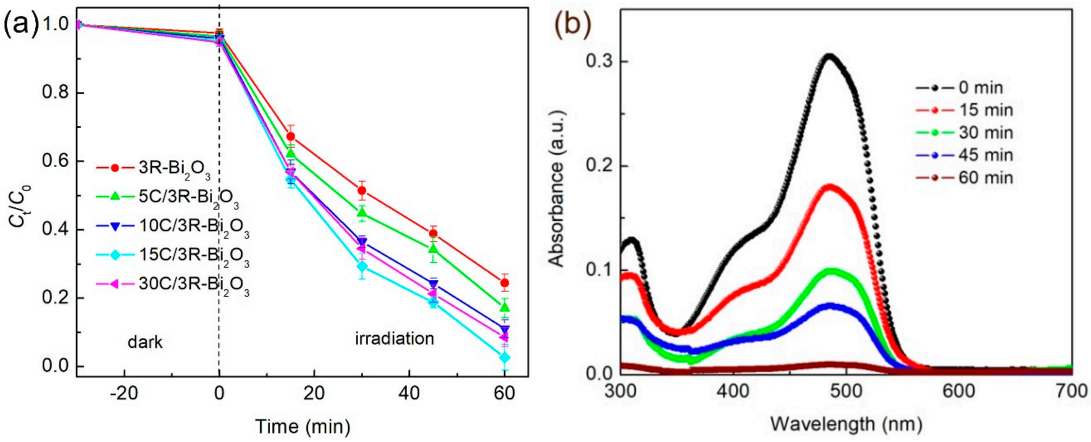

Figure 9. *Cont.*

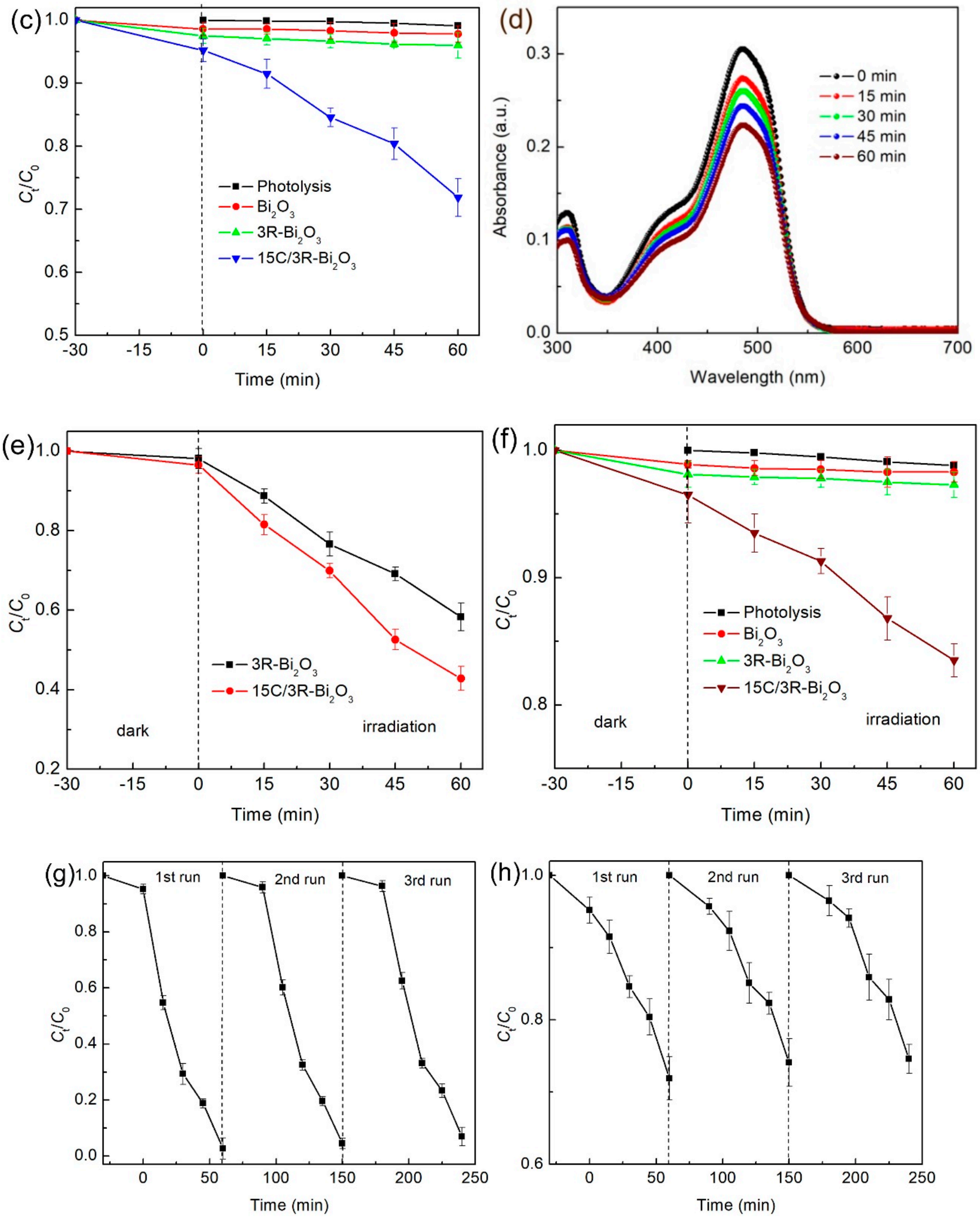

Figure 9. (**a**) Time-dependent photocatalytic degradation of AO7 using Bi_2O_3 and CQDs/3R-Bi_2O_{3-x} samples under simulated sunlight irradiation; (**b**) UV-vis absorption spectra of AO7 degraded by the 15C/3R-Bi_2O_{3-x} under simulated sunlight irradiation; (**c**) Time-dependent photocatalytic degradation of AO7 using Bi_2O_3, 3R-Bi_2O_{3-x} and 15C/3R-Bi_2O_{3-x} samples under NIR light irradiation (**d**) UV-vis absorption spectra of AO7 degraded by the 15C/3R-Bi_2O_{3-x} sample under NIR light irradiation; (**e**,**f**) Time-dependent photocatalytic degradation of phenol using 3R-Bi_2O_{3-x} and 15C/3R-Bi_2O_{3-x} samples under simulated sunlight and NIR light irradiation, respectively; (**g**,**h**) Photocatalytic degradation of AO7 over the 15C/3R-Bi_2O_{3-x} sample during three cycles under simulated sunlight and NIR light irradiation, respectively. Initial conditions: *C*(catalysts) = 0.5 g/L, *C*(phenol) = 5 mg/L, *C*(AO7) = 5 mg/L, pH(AO7) ≈ 6.7, pH(phenol) ≈ 6.2, volume of reaction solution = 200 mL.

2.6. Photogenerated Charges Performance

The photogenerated charge separation of the samples was examined by photoelectrochemical measurements. Figure 10a displays the photocurrent response plots of the composites with intermittent on/off cycles of simulated sunlight illumination. The reproducible photocurrent response curves can be detected in each on-off cycle. It is found that Bi_2O_3 exhibits low photocurrent density, and the photocurrent of the 3R-$Bi_2O_{3\text{-}x}$ sample is much higher than that of Bi_2O_3. This suggests the effective separation of photogenerated charges in the $Bi_2O_{3\text{-}x}$ sample. Compared with Bi_2O_3 and 3R-$Bi_2O_{3\text{-}x}$, the 15C/3R-$Bi_2O_{3\text{-}x}$ sample possesses the highest photocurrent density, indicating that separation of photogenerated charges can be further promoted by the decoration of CQDs. Figure 10b displays the EIS spectra of Bi_2O_3, 3R-$Bi_2O_{3\text{-}x}$ and 15C/3R-$Bi_2O_{3\text{-}x}$. The smaller semicircle radius is observed for the 15C/3R-$Bi_2O_{3\text{-}x}$ sample, suggesting that it exhibits the lowest interface charge-transfer resistance [58,59].

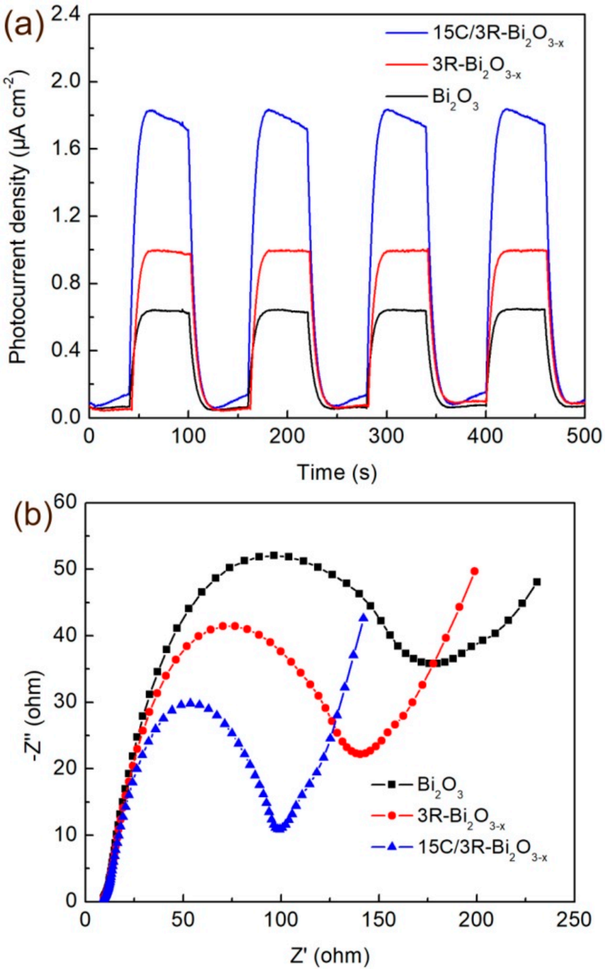

Figure 10. (**a**) Transient photocurrent response curves; and (**b**) Electrochemical impedance spectra (EIS) of Bi_2O_3, 3R-$Bi_2O_{3\text{-}x}$ and 15C/3R-$Bi_2O_{3\text{-}x}$ samples.

2.7. Photocatalytic Mechanism

To clarify the photocatalytic mechanism, the active species involved in the photocatalytic degradation process were evaluated by trapping experiments [60,61]. Figure 11a shows the effect of $AgNO_3$ (scavenger for electrons; e^-), ethanol (scavenger for hydroxyl radicals; •OH), EDTA (scavenger for holes; h^+), KI (scavenger for hydroxyl radicals and holes) and N_2 purging on the AO7 degradation over the 15C/3R-$Bi_2O_{3\text{-}x}$ sample under simulated sunlight irradiation. In addition, the N_2 purging frequently used to expel the O_2 molecules dissolved in reaction solution, and therefore the effect of superoxide (•O_2^-)and/or hydrogen peroxide (H_2O_2), which are derived from the reaction between dissolved O_2 and photogenerated electrons, on the photocatalytic reaction can be determined. The degradation efficiency of AO7 is about ~97% in the absence of scavengers, which decreases to 3.5%, ~48%, ~55%, ~81% and ~88% with the introduction of KI, ethanol, EDTA, $AgNO_3$ and N_2 purging, respectively. This reveals that •OH and h^+ are the major active species responsible for the degradation of dye. On the other hand, e^-, $•O_2^-$ and/or H_2O_2 play relatively minor role in the photocatalytic reaction. The photocatalytic degradation activity of the 15C/3R-$Bi_2O_{3\text{-}x}$ sample with the addition of different scavengers under NIR light irradiation is presented in Figure 11b. One can see that •OH and h^+ also exhibit remarkable role during the photocatalytic process.

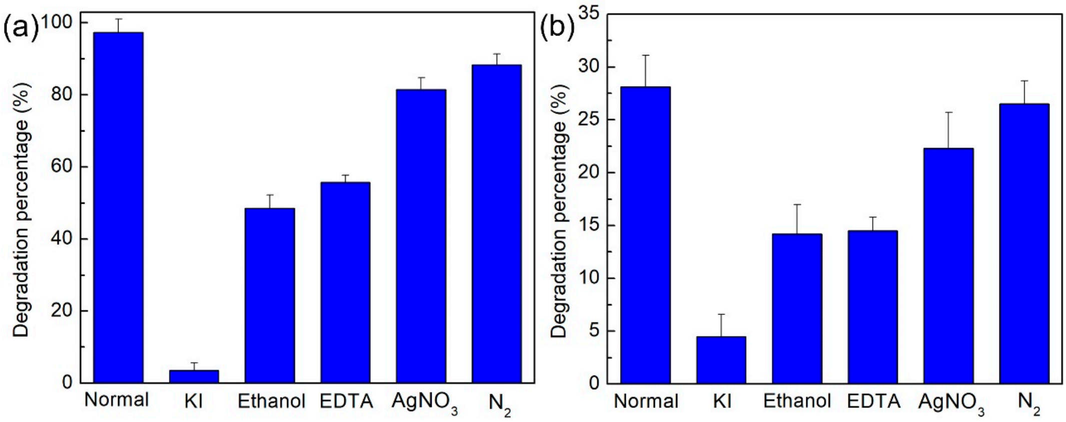

Figure 11. (**a**,**b**) Effects of KI, ethanol, EDTA, $AgNO_3$ and N_2 purging on the photocatalytic degradation of AO7 over the 15C/3R-$Bi_2O_{3\text{-}x}$ sample under simulated sunlight and NIR light irradiation, respectively; Initial conditions: *C* (catalysts) = 0.5 g/L, *C* (AO7) = 5 mg/L, *C* ($AgNO_3$) = 2 mmol/L, *C* (ethanol) = 10% by volume, *C* (KI) = 2 mmol/L, *C* (EDTA) = 2 mmol/L, N_2 purging = 0.1 L/min, volume of reaction solution = 200 mL.

To clarify the catalytic mechanism of photocatalysts, it is necessary to estimate their energy-band potentials. The energy-band structure of 3R-$Bi_2O_{3\text{-}x}$ was investigated through Mott-Schottky (M-S) measurement as described in the literature [62,63], and its flat band potential was estimated according to the Mott-Schottky formula:

$$\frac{1}{C^2} = \left(\frac{2}{e\varepsilon_r\varepsilon_0 N_d A}\right)\left(V - V_{FB} - \frac{kT}{e}\right)$$

where *C* is the space charge capacitance, *e*, ε_r and ε_0 are the electron charge, relative permittivity and vacuum permittivity, respectively, N_d, *A*, *V*, V_{FB}, *k*, and *T* are the majority carrier density, electrode surface area, applied potential, flat band potential, Boltzmann constant and absolute temperature, respectively. In this work, the space charge capacitance of 3R-$Bi_2O_{3\text{-}x}$ is tested though the electrochemical impedance measurement. The M-S curve of 3R-$Bi_2O_{3\text{-}x}$ tested at 1000 Hz is presented in Figure 12, from which the flat band potential (V_{FB}) can be estimated, by extrapolating the linear portion of the curves to the potential axis, to be 2.51 V vs. SCE (3.17 V vs. NHE). Moreover, the negative slope of the M-S curve reveals that $Bi_2O_{3\text{-}x}$ is a p-type semiconductor, which is agree with previous reports [64,65]. Generally, it has been demonstrated that the top edge of the VB is very close to the flat band potential, and the gap between them can be neglected [66]. As a result, the conduction band (CB) and valence band (VB) potentials of the 3R-$Bi_2O_{3\text{-}x}$ can be calculated to be +0.34 and +3.17 V vs. NHE, respectively.

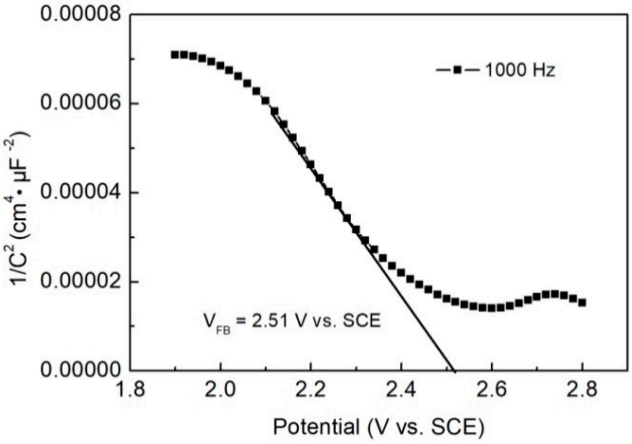

Figure 12. Mott-Schottky curve of the 15C/3R-Bi_2O_{3-x} sample.

Figure 13a shows the simulated-sunlight-driven photocatalytic mechanism of the 15C/3R-Bi_2O_{3-x} sample for the degradation of the dye. Under the irradiation of simulated sunlight, the electrons in the VB of Bi_2O_3 can be excited to its CB, leading to the generation of photogenerated electrons and holes. It is known that a great deal of photogenerated charges tend to recombine during the migration process, giving raise to the reduction of photocatalytic efficiency. After the introduction of surface oxygen vacancies on Bi_2O_3 through $NaBH_4$ reduction, they can act as excellent electron donors to promote an efficient migration and separation of photogenerated charges, thus leading to the improvement of photocatalytic efficiency [33]. On the other hand, the surface vacancy states are always introduced into the band gap of Bi_2O_3, which is beneficial to narrow the band gap and broaden photoresponse region (as evidence by Figure 6b).

Meanwhile, the CQDs decorated on the surface of the Bi_2O_{3-x} can be also excited to generate photoexcited electrons, and the excited CQDs are known to be the electron acceptors and dye adsorption sites [38,39]. As a result, the photogenerated electrons of CQDs can transfer to the CB of Bi_2O_{3-x}, inversely the photogenerated e^- trapped by the surface oxygen vacancies of the Bi_2O_{3-x} will transfer to CQDs. In this process, the migration and separation of photoexcited charges can be further promoted. More importantly, it is generally accepted that CQDs are an outstanding up-converted photoluminescence material. The up-converted PL spectra of obtained CQDs under the excitation wavelength > 800 nm (NIR light range) are shown in Figure 13b. It is observed that the up-converted emissions are located at shorter wavelengths in the range of 300–650 nm. As shown in Figure 6a, the 3R-Bi_2O_{3-x} can effectively response to the light with the wavelength shorter than ~450 nm. As a result, a part of the up-converted emissions of CQDs can in turn excite Bi_2O_{3-x} to generate additional photoexcited charges, further extending the photoresponse range of Bi_2O_3 to the NIR light region.

In addition, the redox ability of photoinduced charges is thought to be another crucial parameter for understanding the photocatalytic mechanism. Based on the M-S investigation, the CB and VB potentials of the as-prepared 3R-Bi_2O_{3-x} sample are evaluated to be +0.34 and +3.17 V vs. NHE, respectively. It is demonstrated that the photogenerated holes of the Bi_2O_{3-x} exhibits high photocatalytic oxidation ability for the degradation of dyes due to its deep valence band. Furthermore, the VB potential of the Bi_2O_{3-x} is positive to the redox potential of $OH^-/\bullet OH$ (+1.99 V vs. NHE) [67,68], indicating the VB holes of Bi_2O_{3-x} can react with OH^- to generate $\bullet OH$. On the other hand, the CB potential of 3R-Bi_2O_{3-x} sample is positive to the redox potential of $O_2/\bullet O_2^-$ (0.13 V vs. NHE), but negative to that of O_2/H_2O_2 (+0.695 vs. NHE). This indicates that the photogenerated e^- can reduce O_2 to generate H_2O_2 instead of $\bullet O_2^-$. Furthermore, the role of photogenerated electrons of Bi_2O_{3-x} for the degradation of dye is also demonstrated.

Figure 13c shows the NIR-light-driven photocatalytic mechanism of the 15C/3R-Bi_2O_{3-x} sample for the degradation of dye. Under illumination of NIR light, only CQDs in the 15C/3R-Bi_2O_{3-x} sample can be excited because Bi_2O_{3-x} cannot absorb NIR light (>800 nm). The photogenerated charges migration and up-converted excitation of CQDs in this process are similar to those with the irradiation of simulated sunlight. Therefore, the less photogenerated charges are generated under NIR light irradiation than under simulated sunlight irradiation. This leads to a relatively weak NIR-light-driven photocatalytic activity.

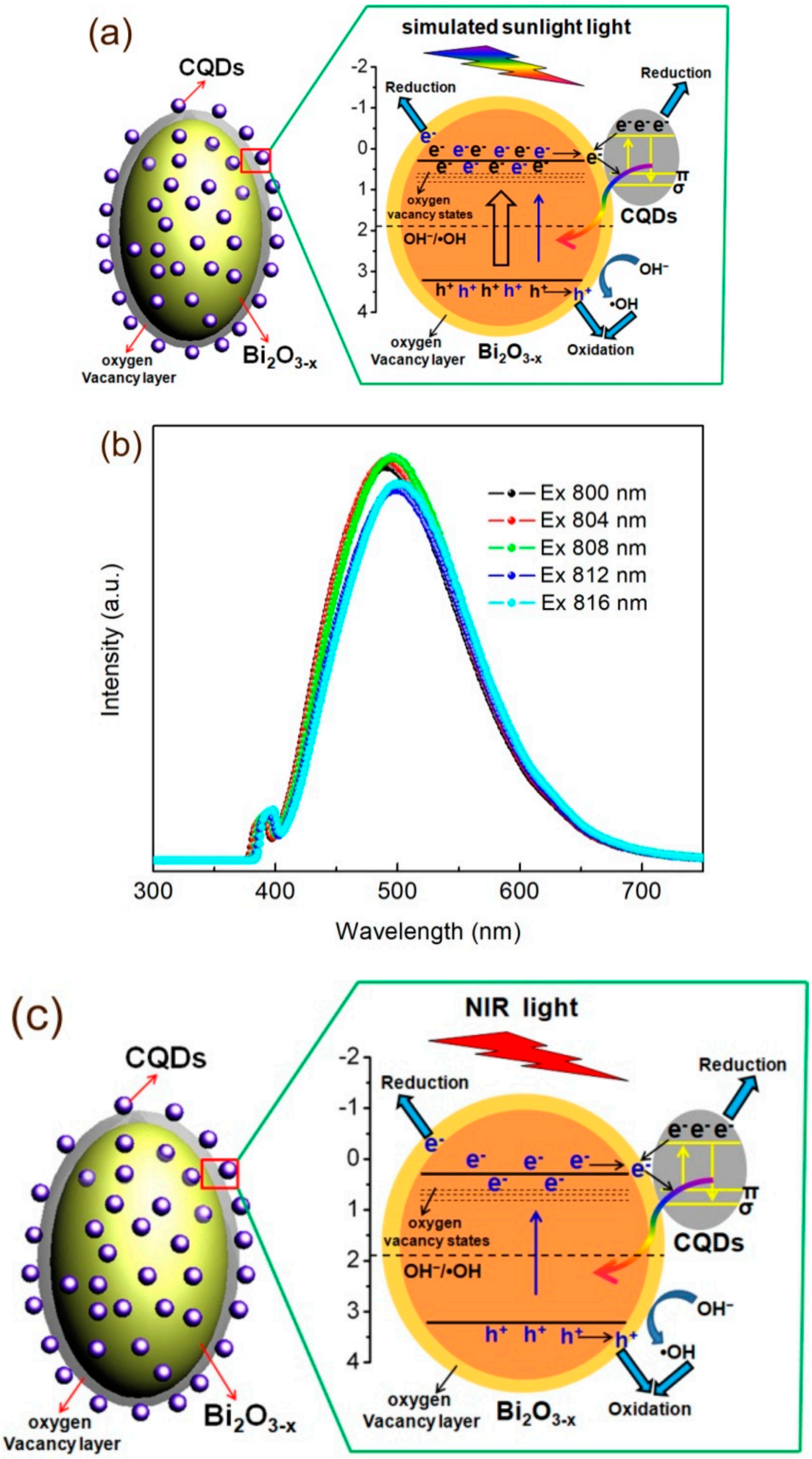

Figure 13. (**a**) A possible photocatalytic mechanism of AO7 degradation over the 15C/3R-Bi_2O_{3-x} sample under simulated sunlight irradiation; (**b**) Up-converted photoluminescence (PL) spectra of CQDs excited by different wavelengths; (**c**) A possible photocatalytic mechanism of AO7 degradation over the 15C/3R-Bi_2O_{3-x} sample under NIR light irradiation.

3. Materials and Methods

3.1. Fabrication of CQDs

The CQDs were obtained through a hydrothermal route. Glucose (1 g) was dissolved into distilled water (80 mL) to obtain a homogeneous solution. Then, the solution was treated under a hydrothermal condition (180 °C, 4 h). After that, the solution was given a filter treatment, and then a reddish-brown CQDs suspension was obtained.

3.2. Fabrication of CQDs/$Bi_2O_{3\text{-}x}$ Composites

The synthesis of CQDs/$Bi_2O_{3\text{-}x}$ composites was achieved in three steps, as shown in Figure 14. Firstly, the Bi_2O_3 was obtained through a polyacrylamide gel route. A certain amount (0.015 mol) of $Bi(NO_3)_3{\bullet}5H_2O$ was introduced into the dilute nitric acid solution (20 mL). Under magnetic stirring, EDTA (0.0225 mol), glucose (20 g) and acrylamide (0.135 mol) were dissolved in above solution, and then a certain volume (~65 mL) of distilled water was added to make a total volume of 100 mL. After that, the mixture was heated at 80 °C to obtain gel. The gel was dried at 120 °C for 24 h, and then heat-treated at 650 °C for 3 h to yield Bi_2O_3. Secondly, the $Bi_2O_{3\text{-}x}$ sample was prepared by a $NaBH_4$ reduction route. The Bi_2O_3 was introduced into $NaBH_4$ solution with certain concentration (1, 1.5, 3 and 6 mmol/L) in ice-water bath under constant magnetic stirring. After reaction for 10 min, the $Bi_2O_{3\text{-}x}$ sample was centrifuged, washed and then dried at 60 °C for 4 h. By changing the $NaBH_4$ concentration (1, 1.5, 3 and 6 mmol/L), different reduced samples of 1R-$Bi_2O_{3\text{-}x}$, 1.5R-$Bi_2O_{3\text{-}x}$, 3R-$Bi_2O_{3\text{-}x}$ and 6R-$Bi_2O_{3\text{-}x}$ were obtained. Thirdly, a hydrothermal method was employed to prepare the CQDs/$Bi_2O_{3\text{-}x}$ composites. 0.1 g of the 3R-$Bi_2O_{3\text{-}x}$ sample was added into distilled water (70 mL), followed by magnetic stirring for 0.5 h. Subsequently, a certain volume of CQDs suspension was dropped into above mixture. After that, the solution was transferred into the Teflon-lined autoclave, which was hydrothermally treated at 130 °C for 4 h. The sample was obtained by centrifugation, washed, and then dried at 60 °C for 4 h to yield the CQDs/$Bi_2O_{3\text{-}x}$ composites. To study the impact of the CQDs content on the photocatalytic performance of the composites, a series of the CQDs/$Bi_2O_{3\text{-}x}$ composites were obtained by adjusting the volumes of CQDs suspension (5, 10, 15 and 30 mL), and the samples were correspondingly named as 5C/3R-$Bi_2O_{3\text{-}x}$, 10C/3R-$Bi_2O_{3\text{-}x}$, 15C/3R-$Bi_2O_{3\text{-}x}$ and 30C/3R-$Bi_2O_{3\text{-}x}$.

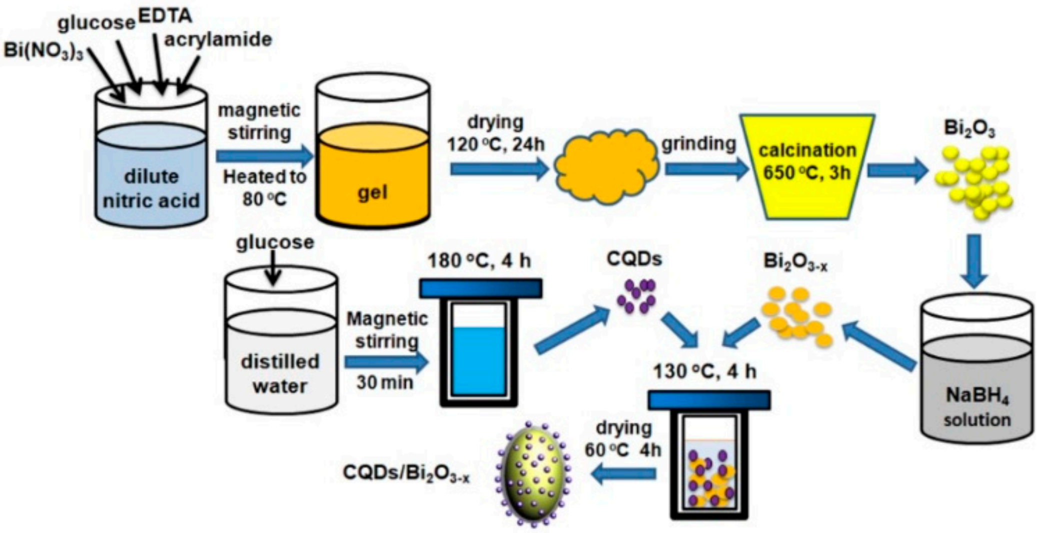

Figure 14. Schematic illustration of the preparation process of the CQDs/$Bi_2O_{3\text{-}x}$.

3.3. Photocatalytic Measurement

The photocatalytic performances of the composites were examined toward the degradation of AO7 and phenol under simulated sunlight (300-W xenon lamp) and NIR light (300-W xenon lamp with a 800 nm cut-off filter) irradiation. In a typical photocatalytic process, 0.1 g of the catalysts was introduced into AO7 or phenol solution (200 mL, 5 mg/L). After 0.5 h magnetic stirring in dark, an adsorption-desorption equilibrium between sample and dye was achieved. Subsequently, the light source was turned on to start photocatalytic reaction. In the photocatalytic process, 3 mL of reaction solution was taken and centrifuged to separate the catalyst. The AO7 or phenol concentration of the reaction solution was obtained by an ultraviolet-visible (UV-vis) spectrophotometer at λ_{AO7} = 484 nm and λ_{phenol} = 270 nm. To study the photocatalytic stability of the samples, the recycling photocatalytic degradation experiments were performed. After each photocatalytic experiment, the catalysts were collected and recovered by washing with deionized water and drying. The recovered catalysts were used to degrade the new AO7 solution under the same conditions. For the radical-trapping experiment, $AgNO_3$ (2 mmol/L), ethanol (10% by volume), KI (2 mmol/L), EDTA (2 mmol/L) and N_2 purging (0.1 L/min) were separately introduced into the reaction solution under the same photocatalytic conditions.

3.4. Characterization

X-ray powder diffraction (XRD) and Fourier transform infrared spectroscopy (FTIR) were used to examine the phase purity and functional groups of the as-prepared photocatalysts. The XRD and FTIR investigation were performed on a D8 Advance X-ray diffractometer (Bruker AXS, Karlsruhe, Germany) and a Spectrum Two FTIR spectrophotometer (PerkinElmer, Waltham, MA, USA), respectively. Field-emission transmission electron microscopy (TEM) was employed to observe the morphology and microstructure of the photocatalysts on a JEM-1200EX transmission electron microscope (JEOL Ltd., Tokyo, Japan). The X-ray photoelectron spectroscopy (XPS) was employed to determine the chemical states of the surface elements for the photocatalysts on a PHI-5702 multi-functional X-ray photoelectron spectrometer (Physical Electronics, Chanhassen, MN, USA). The photoluminescence (PL) spectra of the photocatalysts were obtained by a fluorescence spectrophotometer (Shimadzu, Kyoto, Japan). The UV-vis diffuse reflectance spectra of the photocatalysts were determined by a TU-1901 double beam UV-Vis spectrophotometer (Beijing Purkinje General Instrument Co. Ltd., Beijing, China) with $BaSO_4$ as a reference. The electrochemical workstation (CHI 660C, Shanghai Chenhua Instrument Co. Ltd., Shanghai, China) with a three-electrode system was adopted to achieve the transient photocurrent response and electrochemical impedance spectroscopy (EIS) measurements. The working electrode preparation and measurement procedures were the same as those previously reported [3]. The photocurrent response test was performed under the irradiation of simulated sunlight (300-W xenon lamp).

4. Conclusions

The Bi_2O_{3-x} with surface oxygen vacancies was prepared via a $NaBH_4$ reduction route. Then, the CQDs were successfully deposited onto the surface of Bi_2O_{3-x} to prepare the CQDs/Bi_2O_{3-x} composites. The photocatalytic AO7 degradation experiments confirm that the simulated-sunlight-driven photocatalytic performances of the samples are closely related to the concentration of $NaBH_4$ and content of CQDs. The introduction of surface oxygen vacancies effectively improves the photocatalytic activity of Bi_2O_3 under simulated sunlight irradiation. Moreover, the photocatalytic efficiency of the Bi_2O_{3-x} can be further enhanced by the decoration of CQDs, and the highest AO7 degradation percentage of ~97% has been achieved over the 15C/3R-Bi_2O_{3-x} sample within 60 min simulated sunlight irradiation. The NIR-light-driven photocatalytic activity of the CQDs/Bi_2O_{3-x} samples is also found. The •OH and h^+ play a significant role in the simulated-sunlight and NIR-light-driven photocatalytic reaction over the CQDs/Bi_2O_{3-x} composites. The surface oxygen vacancies of the Bi_2O_{3-x} can act as electrons acceptors, which inhibits the recombination of photogenerated charges. Moreover, the surface oxygen-vacancy states can narrow the band gap of Bi_2O_3. On the other hand, the separation and transference of photogenerated charges can be further enhanced due to the good electrical conductivity of CQDs. The outstanding up-converted photoluminescence property of CQDs enables the CQDs/Bi_2O_{3-x} composites to make use of NIR light and extend the photoresponse region of Bi_2O_3. As a result, the synergistic effect of surface oxygen vacancies and CQDs lead to the excellent photocatalytic activity of the CQDs/Bi_2O_{3-x} composites.

Author Contributions: T.X. and X.S. designed the experiment; X.S., L.D., Y.Z. and H.L. carried out the experiments; T.X., X.S., J.M. and L.D. analyzed the result; T.X. and H.Y. drafted and revised the manuscript. All authors commented and approved the final manuscript.

Funding: This work was supported by the National Natural Science Foundation of China (Grant No. 51602170), the Natural Science Foundation of Qinghai, China (Grant No.2016-ZJ-954Q), "Chun Hui" Program of Ministry of Education of China (Grant No. Z2016075) and the Youth Science Foundation of Qinghai Normal University (Grant No. 2019zr003).

Conflicts of Interest: The authors declare no conflict of interest.

References

1. Tokunaga, S.; Kato, H.; Kudo, A. Selective preparation of monoclinic and tetragonal $BiVO_4$ with scheelite structure and their photocatalytic properties. *Chem. Mater.* **2001**, *13*, 4624–4628. [CrossRef]
2. Saison, T.; Chemin, N.; Chaneac, C.; Durupthy, O.; Ruaux, V.; Mariey, L.; Mauge, F.; Beaunier, P.; Jolivet, J.P. Bi_2O_3, $BiVO_4$, and Bi_2WO_6: Impact of surface properties on photocatalytic activity under visible light. *J. Phys. Chem. C* **2011**, *115*, 5657–5666. [CrossRef]
3. Di, L.; Yang, H.; Xian, T.; Liu, X.; Chen, X. Photocatalytic and photo-Fenton catalytic degradation activities of Z-scheme $Ag_2S/BiFeO_3$ heterojunction composites under visible-light irradiation. *Nanomaterials* **2019**, *9*, 399. [CrossRef] [PubMed]
4. Chen, J.; Guan, M.; Cai, W.; Guo, J.; Xiao, C.; Zhang, G. The dominant {001} facet-dependent enhanced visible-light photoactivity of ultrathin BiOBr nanosheets. *Phys. Chem. Chem. Phys.* **2014**, *16*, 20909–20914. [CrossRef]
5. Yan, Y.; Yang, H.; Yi, Z.; Xian, T. $NaBH_4$-reduction induced evolution of Bi nanoparticles from BiOCl nanoplates and construction of promising Bi@BiOCl hybrid photocatalysts. *Catalysts* **2019**, *9*, 795. [CrossRef]
6. Yi, Z.; Zeng, Y.; Wu, H.; Chen, X.; Fan, Y.; Yang, H.; Tang, Y.; Yi, Y.; Wang, J.; Wu, P. Synthesis, surface properties, crystal structure and dye-sensitized solar cell performance of TiO_2 nanotube arrays anodized under different parameters. *Results Phys.* **2019**, *15*, 102609. [CrossRef]
7. Yi, Z.; Li, X.; Wu, H.; Chen, X.; Yang, H.; Tang, Y.; Yi, Y.; Wang, J.; Wu, P. Fabrication of ZnO@Ag_3PO_4 core-shell nanocomposite arrays as photoanodes and their photoelectric properties. *Nanomaterials* **2019**, *9*, 1254. [CrossRef]
8. Shi, Y.; Luo, L.; Zhang, Y.; Chen, Y.; Wang, S.; Li, L.; Long, Y.; Jiang, F. Synthesis and characterization of α/β-Bi_2O_3 with enhanced photocatalytic activity for 17α-ethynylestradiol. *Ceram. Int.* **2017**, *43*, 7627–7635. [CrossRef]
9. Wang, Q.; Shi, X.; Liu, E.; Crittenden, J.C.; Ma, X.; Zhang, Y.; Cong, Y. Facile synthesis of AgI/BiOI-Bi_2O_3 multi-heterojunctions with high visible light activity for Cr (VI) reduction. *J. Hazard. Mater.* **2016**, *317*, 8–16. [CrossRef]
10. Vignesh, K.; Priyanka, R.; Rajarajan, M.; Suganthi, A. Photoreduction of Cr (VI) in water using Bi_2O_3–ZrO_2 nanocomposite under visible light irradiation. *Mater. Sci. Eng. B* **2013**, *178*, 149–157. [CrossRef]
11. Muruganandham, M.; Amutha, R.; Lee, G.J.; Hsieh, S.H.; Wu, J.J.; Sillanpää, M. Facile fabrication of tunable Bi_2O_3 self-assembly and its visible light photocatalytic activity. *J. Phys. Chem. C* **2012**, *116*, 12906–12915. [CrossRef]
12. Xiong, M.; Chen, L.; Yuan, Q.; He, J.; Luo, S.L.; Au, C.T.; Yin, S.F. Controlled synthesis of graphitic carbon nitride/beta bismuth oxide composite and its high visible-light photocatalytic activity. *Carbon* **2015**, *86*, 217–224. [CrossRef]
13. Iyyapushpam, S.; Nishanthi, S.T.; Padiyan, D.P. Photocatalytic degradation of methyl orange using α-Bi_2O_3 prepared without surfactant. *J. Alloys Compd.* **2013**, *563*, 104–107. [CrossRef]
14. Xiao, X.; Hu, R.; Liu, C.; Xing, C.; Qian, C.; Zuo, X.; Nan, J.; Wang, L. Facile large-scale synthesis of β-Bi_2O_3 nanospheres as a highly efficient photocatalyst for the degradation of acetaminophen under visible light irradiation. *Appl. Catal. B Environ.* **2013**, *140*, 433–443. [CrossRef]

15. Gurunathan, K. Photocatalytic hydrogen production using transition metal ions-doped γ-Bi_2O_3 semiconductor particles. *Int. J. Hydrogen Energy* **2004**, *29*, 933–940. [CrossRef]
16. Zhu, S.; Lu, L.; Zhao, Z.; Wang, T.; Liu, X.; Zhang, H.; Dong, F.; Zhang, Y. Mesoporous Ni-doped δ-Bi_2O_3 microspheres for enhanced solar-driven photocatalysis: A combined experimental and theoretical investigation. *J. Phys. Chem. C* **2017**, *121*, 9394–9401. [CrossRef]
17. Gualtieri, A.F.; Immovilli, S.; Prudenziati, M. Powder X-ray diffraction data for the new polymorphic compound ω-Bi_2O_3. *Powder Diffr.* **1997**, *12*, 90–92. [CrossRef]
18. Cornei, N.; Tancret, N.; Abraham, F.; Mentré, O. New ε-Bi_2O_3 metastable polymorph. *Inorg. Chem.* **2006**, *45*, 4886–4888. [CrossRef]
19. Hashimoto, T.; Ohta, H.; Nasu, H.; Ishihara, A. Preparation and photocatalytic activity of porous Bi_2O_3 polymorphisms. *Int. J. Hydrogen Energy* **2016**, *41*, 7388–7392. [CrossRef]
20. Zhang, L.; Wang, W.; Yang, J.; Chen, Z.; Zhang, W.; Zhou, L.; Liu, S. Sonochemical synthesis of nanocrystallite Bi_2O_3 as a visible-light-driven photocatalyst. *Appl. Catal. A Gen.* **2006**, *308*, 105–110. [CrossRef]
21. Hernández-Gordillo, A.; Medina, J.C.; Bizarro, M.; Zanella, R.; Monroy, B.M.; Rodil, S.E. Photocatalytic activity of enlarged microrods of α-Bi_2O_3 produced using ethylenediamine-solvent. *Ceram. Int.* **2016**, *42*, 11866–11875. [CrossRef]
22. Wang, C.; Shao, C.; Wang, L.; Zhang, L.; Li, X.; Liu, Y. Electrospinning preparation, characterization and photocatalytic properties of Bi_2O_3 nanofibers. *J. Colloid Interface Sci.* **2009**, *333*, 242–248. [CrossRef]
23. Li, Y.; Yang, F.; Yu, Y. Enhanced photocatalytic activity of α-Bi_2O_3 with high electron-hole mobility by codoping approach: A first-principles study. *Appl. Surf. Sci.* **2015**, *358*, 449–456. [CrossRef]
24. Jiang, H.Y.; Cheng, K.; Lin, J. Crystalline metallic Au nanoparticle-loaded α-Bi_2O_3 microrods for improved photocatalysis. *Phys. Chem. Chem. Phys.* **2012**, *14*, 12114–12121. [CrossRef] [PubMed]
25. Yu, P.; Chen, X.; Yi, Z.; Tang, Y.; Yang, H.; Zhou, Z.; Duan, T.; Cheng, S.; Zhang, J.; Yi, Y. A numerical research of wideband solar absorber based on refractory metal from visible to near infrared. *Opt. Mater.* **2019**, *97*, 109400. [CrossRef]
26. Liang, C.; Yi, Z.; Chen, X.; Tang, Y.; Yi, Y.; Zhou, Z.; Wu, X.; Huang, Z.; Yi, Y.; Zhang, G. Dual-band infrared perfect absorber based on a Ag-dielectric-Ag multilayer films with nanoring grooves arrays. *Plasmonics* **2019**. [CrossRef]
27. Zhang, J.; Hu, Y.; Jiang, X.; Chen, S.; Meng, S.; Fu, X. Design of a direct Z-scheme photocatalyst: Preparation and characterization of Bi_2O_3/g-C_3N_4 with high visible light activity. *J. Hazard. Mater.* **2014**, *280*, 713–722. [CrossRef]
28. Pugazhenthiran, N.; Sathishkumar, P.; Murugesan, S.; Anandan, S. Effective degradation of acid orange 10 by catalytic ozonation in the presence of Au-Bi_2O_3 nanoparticles. *Chem. Eng. J.* **2011**, *168*, 1227–1233. [CrossRef]
29. Liang, J.; Zhu, G.; Liu, P.; Luo, X.; Tan, C.; Jin, L.; Zhou, J. Synthesis and characterization of Fe-doped β-Bi_2O_3 porous microspheres with enhanced visible light photocatalytic activity. *Superlattices Microstruct.* **2014**, *72*, 272–282. [CrossRef]
30. Liu, J.; Zou, S.; Wang, H.; Xiao, L.; Zhao, H.; Fan, J. Synergistic effect between Pt and Bi_2O_{3-x} for efficient room-temperature alcohol oxidation under base-free aqueous conditions. *Catal. Sci. Technol.* **2017**, *7*, 1203–1210. [CrossRef]
31. Zhao, X.; Yang, H.; Zhang, H.; Cui, Z.; Feng, W. Surface-disorder-engineering-induced enhancement in the photocatalytic activity of $Bi_4Ti_3O_{12}$ nanosheets. *Desalin. Water Treat.* **2019**, *145*, 326–336. [CrossRef]
32. Pan, X.; Yang, M.Q.; Fu, X.; Zhang, N.; Xu, Y.J. Defective TiO_2 with oxygen vacancies: Synthesis, properties and photocatalytic applications. *Nanoscale* **2013**, *5*, 3601–3614. [CrossRef] [PubMed]
33. Wang, S.; Yang, H.; Wang, X.; Feng, W. Surface disorder engineering of flake-like Bi_2WO_6 crystals for enhanced photocatalytic activity. *J. Electron. Mater.* **2019**, *48*, 2067–2076. [CrossRef]
34. Li, D.; Haneda, H.; Labhsetwar, N.K.; Hishita, S.; Ohashi, N. Visible-light-driven photocatalysis on fluorine-doped TiO_2 powders by the creation of surface oxygen vacancies. *Chem. Phys. Lett.* **2005**, *401*, 579–584. [CrossRef]
35. Nakamura, I.; Negishi, N.; Kutsuna, S.; Ihara, T.; Sugihara, S.; Takeuchi, K. Role of oxygen vacancy in the plasma-treated TiO_2 photocatalyst with visible light activity for NO removal. *J. Mol. Catal. A Chem.* **2000**, *161*, 205–212. [CrossRef]

36. Li, H.; He, X.; Kang, Z.; Huang, H.; Liu, Y.; Liu, J.; Lian, S.; Tsang, C.H.A.; Yang, X.; Lee, S.T. Water-soluble fluorescent carbon quantum dots and photocatalyst design. *Angew. Chem. Int. Ed.* **2010**, *49*, 4430–4434. [CrossRef]
37. Lim, S.Y.; Shen, W.; Gao, Z. Carbon quantum dots and their applications. *Chem. Soc. Rev.* **2015**, *44*, 362–381. [CrossRef]
38. Gao, H.; Zheng, C.; Yang, H.; Niu, X.; Wang, S. Construction of a CQDs/Ag_3PO_4/$BiPO_4$ heterostructure photocatalyst with enhanced photocatalytic degradation of rhodamine B under simulated solar irradiation. *Micromachines* **2019**, *10*, 557. [CrossRef]
39. Kulandaivalu, T.; Rashid, S.A.; Sabli, N.; Tan, T.L. Visible light assisted photocatalytic reduction of CO_2 to ethane using CQDs/Cu_2O nanocomposite photocatalyst. *Diam. Relat. Mater.* **2019**, *91*, 64–73. [CrossRef]
40. Han, M.; Zhu, S.; Lu, S.; Song, Y.; Feng, T.; Tao, S.; Liu, J.; Yang, B. Recent progress on the photocatalysis of carbon dots: Classification, mechanism and applications. *Nano Today* **2018**, *19*, 201–218. [CrossRef]
41. Gao, H.; Wang, F.; Wang, S.; Wang, X.; Yi, Z.; Yang, H. Photocatalytic activity tuning in a novel Ag_2S/CQDs/$CuBi_2O_4$ composite: Synthesis and photocatalytic mechanism. *Mater. Res. Bull.* **2019**, *115*, 140–149. [CrossRef]
42. De, B.; Karak, N. Recent progress in carbon dot-metal based nanohybrids for photochemical and electrochemical applications. *J. Mater. Chem. A* **2017**, *5*, 1826–1859. [CrossRef]
43. Sharma, S.; Mehta, S.K.; Ibahdon, A.O.; Kansal, S.K. Fabrication of novel Carbon Quantum Dots modified Bismuth Oxide (α-Bi_2O_3/C-dots): Material Properties and Catalytic Applications. *J. Colloid Interface Sci.* **2019**, *533*, 227–237. [CrossRef] [PubMed]
44. Shao, B.; Liu, X.; Liu, Z.; Zeng, G.; Liang, Q.; Liang, C.; Cheng, Y.; Zhang, W.; Liu, Y.; Gong, S. A novel double Z-scheme photocatalyst Ag_3PO_4/Bi_2S_3/Bi_2O_3 with enhanced visible-light photocatalytic performance for antibiotic degradation. *Chem. Eng. J.* **2019**, *368*, 730–745. [CrossRef]
45. Luo, D.; Kang, Y. Controlled preparation of fiber-shaped 4-Br/Bi_2O_3 composite photocatalysts with excellent visible-light photocatalytic activity. *J. Mater. Sci.* **2019**, *54*, 1549–1565. [CrossRef]
46. Faisal, M.; Ibrahim, A.A.; Bouzid, H.; Al-Sayari, S.A.; Al-Assiri, M.S.; Ismail, A.A. Hydrothermal synthesis of Sr-doped α-Bi_2O_3 nanosheets as highly efficient photocatalysts under visible light. *J. Mol. Catal. A Chem.* **2014**, *387*, 69–75. [CrossRef]
47. Singh, V.K.; Yadav, P.K.; Chandra, S.; Bano, D.; Talat, M.; Hasan, S.H. Peroxidase mimetic activity of fluorescent NS-carbon quantum dots and their application in colorimetric detection of H_2O_2 and glutathione in human blood serum. *J. Mater. Chem. B* **2018**, *6*, 5256–5268. [CrossRef]
48. Ren, H.; Ge, L.; Guo, Q.; Li, L.; Hu, G.; Li, J. The enhancement of photocatalytic performance of $SrTiO_3$ nanoparticles via combining with carbon quantum dots. *RSC Adv.* **2018**, *8*, 20157–20165. [CrossRef]
49. Yan, Y.; Yang, H.; Yi, Z.; Wang, X.; Li, R.; Xian, T. Evolution of Bi nanowires from BiOBr nanoplates through a $NaBH_4$ reduction method with enhanced photodegradation performance. *Environ. Eng. Sci.* **2019**. [CrossRef]
50. Imran, M.; Yousaf, A.B.; Farooq, M.; Kasak, P. Enhanced Z-scheme visible light photocatalytic hydrogen production over α-Bi_2O_3/CZS heterostructure. *Int. J. Hydrogen Energy* **2018**, *43*, 4256–4264. [CrossRef]
51. Pooladi, M.; Shokrollahi, H.; Lavasani, S.A.N.H.; Yang, H. Investigation of the structural, magnetic and dielectric properties of Mn-doped $Bi_2Fe_4O_9$ produced by reverse chemical co-precipitation. *Mater. Chem. Phys.* **2019**, *229*, 39–48. [CrossRef]
52. Wang, Y.; Qin, F.; Yi, Z.; Chen, X.; Zhou, Z.; Yang, H.; Liao, X.; Tang, Y.; Yao, W.; Yi, Y. Effect of slit width on surface plasmon resonance. *Results Phys.* **2019**, *15*, 102711. [CrossRef]
53. Liang, C.; Zhang, Y.; Yi, Z.; Chen, X.; Zhou, Z.; Yang, H.; Yi, Y.; Tang, Y.; Yao, W.; Yi, Y. A broadband and polarization-independent metamaterial perfect absorber with monolayer Cr and Ti elliptical disks array. *Results Phys.* **2019**, *15*, 102635. [CrossRef]
54. Zhao, Z.; Zhang, X.; Zhang, G.; Liu, Z.; Qu, D.; Miao, X.; Feng, P.; Sun, Z. Effect of defects on photocatalytic activity of rutile TiO_2 nanorods. *Nano Res.* **2015**, *8*, 4061–4071. [CrossRef]
55. Di, L.; Yang, H.; Xian, T.; Chen, X. Facile synthesis and enhanced visible-light photocatalytic activity of novel p-Ag_3PO_4/n-$BiFeO_3$ heterojunction composites for dye degradation. *Nanoscale Res. Lett.* **2018**, *13*, 257. [CrossRef]
56. Bae, S.; Kim, S.; Lee, S.; Choi, W. Dye decolorization test for the activity assessment of visible light photocatalysts: Realities and limitations. *Catal. Today* **2014**, *224*, 21. [CrossRef]

57. Barbero, N.; Vione, D. Why Dyes Should Not Be Used to Test the Photocatalytic Activity of Semiconductor Oxides. *Environ. Sci. Technol.* **2016**, *50*, 2130. [CrossRef]
58. Zhao, X.; Yang, H.; Cui, Z.; Yi, Z.; Yu, H. Synergistically enhanced photocatalytic performance of $Bi_4Ti_3O_{12}$ nanosheets by Au and Ag nanoparticles. *J. Mater. Sci. Mater. Electron.* **2019**, *30*, 13785–13796. [CrossRef]
59. Xu, T.; Zhang, L.; Cheng, H.; Zhu, Y. Significantly enhanced photocatalytic performance of ZnO via graphene hybridization and the mechanism study. *Appl. Catal. B Environ.* **2011**, *101*, 382–387. [CrossRef]
60. Di, L.; Xian, T.; Sun, X.; Li, H.; Zhou, Y.; Ma, J.; Yang, H. Facile preparation of CNT/Ag_2S nanocomposites with improved visible and NIR light photocatalytic degradation activity and their catalytic mechanism. *Micromachines* **2019**, *10*, 503. [CrossRef]
61. Rivas, J.; Solis, R.R.; Gimeno, O.; Sagasti, J. Photocatalytic elimination of aqueous 2-methyl-4-chlorophenoxyacetic acid in the presence of commercial and nitrogen-doped TiO_2. *Int. J. Environ. Sci. Technol.* **2015**, *12*, 513–526. [CrossRef]
62. Gelderman, K.; Lee, L.; Donne, S.W. Flat-band potential of a semiconductor: Using the Mott-Schottky equation. *J. Chem. Educ.* **2007**, *84*, 685. [CrossRef]
63. Wang, S.; Yang, H.; Yi, Z.; Wang, X. Enhanced photocatalytic performance by hybridization of Bi_2WO_6 nanoparticles with honeycomb-like porous carbon skeleton. *J. Environ. Manag.* **2019**, *248*, 109341. [CrossRef] [PubMed]
64. Wei, N.; Cui, H.; Wang, C.; Zhang, G.; Song, Q.; Sun, W.; Song, X.; Sun, M.; Tian, J. Bi_2O_3 nanoparticles incorporated porous TiO_2 films as an effective p-n junction with enhanced photocatalytic activity. *J. Am. Ceram. Soc.* **2017**, *100*, 1339–1349. [CrossRef]
65. Aggrawal, S.; Chauhan, I.; Mohanty, P. Immobilization of Bi_2O_3 nanoparticles on the cellulose fibers of paper matrices and investigation of its antibacterial activity against E, coli in visible light. *Mater. Express* **2015**, *5*, 429–436. [CrossRef]
66. Yan, Y.; Yang, H.; Yi, Z.; Xian, T.; Wang, X. Direct Z-scheme $CaTiO_3$@ BiOBr composite photocatalysts with enhanced photodegradation of dyes. *Environ. Sci. Pollut. Res.* **2019**, *26*, 29020–29031. [CrossRef]
67. Di, L.; Yang, H.; Xian, T.; Chen, X. Construction of Z-scheme g-C_3N_4/CNT/$Bi_2Fe_4O_9$ composites with improved simulated-sunlight photocatalytic activity for the dye degradation. *Micromachines* **2018**, *9*, 613. [CrossRef]
68. Ye, L.; Liu, J.; Jiang, Z.; Peng, T.; Zan, L. Facets coupling of BiOBr-g-C_3N_4 composite photocatalyst for enhanced visible-light-driven photocatalytic activity. *Appl. Catal. B Environ.* **2013**, *142*, 1–7. [CrossRef]